IIETA International Information and Engineering Technology Association
Advancing the World of Information and Engineering

Mathematical Modelling of Engineering Problems
Vol. 13, No. 1, February, 2026, pp. 210-222
Journal homepage: http://iieta.org/journals/mmep

Numerical and Experimental Study on the Effect of Enhancement Absorber Plates on Solar Collector Efficiency for Comfort Room

Aseel K. Shyaa

Department of Mechanical Engineering, College of Engineering, Mustansiriyah University, Baghdad 14022, Iraq

Corresponding Author Email: aseelk.shyaa@uomustansiriyah.edu.iq

https://doi.org/10.18280/mmep.130119

Received: 2 November 2025
Revised: 9 January 2026
Accepted: 19 January 2026
Available online: 28 February 2026

Keywords:
absorbing plate modifications, enhancement convection heat transfer, comfort room, natural ventilation, ribbed absorber plate, solar chimney

ABSTRACT

The comparison analysis showed that all the modified configurations offered significant improvements compared to the baseline design. The maximum performance was due to the combination of the increase in the mass flow rate and outlet air temperature, resulting in the highest performance of Case 2, with the enhancement rate of about 60 percent in comparison with Case 1. Case 3 provided an enhancement of approximately 35%, which was primarily due to a greater temperature gradient (ΔT) through the collector, even though the enhancement of mass flow was not significant. In Case 4, the temperature rise was the main contributor to almost 50 percent improvement in the system, though a slight resistance that was caused by the addition of rib decreased the mass flow relative to Case 2. The validity of the numerical results was confirmed through experimental testing, where the ribbed configuration of Case 2 attained maximum efficiency of 17.6 percent at maximum solar intensity at 1:00 p.m. The results verify the fact that absorber plate (AP) modification, especially the incorporation of ribs, has the potential to significantly enhance the thermal performance of solar chimneys. The production made ribbed designs featured as a low-cost, scalable, and effective approach to improving natural ventilation systems, which reinforced the larger introduction of sustainable building technologies.

1. INTRODUCTION

A solar chimney (SC) enhances the natural ventilation of a building by encouraging heat transfer through passive solar energy (SE) and convection of heated air. In this process, air is being heated using the SE, and later, lighter air is used in the formation of a draft towards the chimney. When the hot air gains momentum in the chimney, it is removed from the collector, and the cold air is pulled outside. The geometry and the difference in temperature of the SC influence its performance. Also, the thermal energy conversion into mechanical energy occurs at the chimney base [1, 2]. SC performance has been extensively investigated with respect to geometric configuration, heat transfer (HT) mechanisms, and energy storage integration, owing to its potential as a passive ventilation and power-generation system. Several researchers have demonstrated that SC performance is highly sensitive to collector and chimney geometry. Yue et al. [3] studied the effect of SC ventilation. Albaldawi et al. [4] examined the effect of collector inclination angle and reported a noticeable improvement in thermal efficiency at optimized angles. Nie et al. [5] confirmed that three-dimensional simulations provide superior accuracy compared with one-dimensional models when predicting compressible and buoyancy-driven flow inside SCs. Ren et al. [6] further optimized rectangular SCs for greenhouse applications by adjusting collector inclination to reduce local pressure losses and enhance airflow.

Chikere et al. [7] revised preceding investigations upon improving the SC performance and introduced a new approach that combines the solar process with losses of heat energy from flue gas. Dos Santos Bernardes et al. [8] investigated the SC performance and compared several approaches for calculating the collector's heat fluxes (HFs) as well as their effect upon the performance of the SC. Buğutekin [9] studied the SC performance. Findings showed that the ideal height was 0.05 m. Moreover, the system's performance is enhanced by the thermal mass of the ground. During the day, solar radiation (SR) warms the ground, which accumulates heat. At night, this stored heat is released to the atmosphere of the collector, thereby enhancing the performance of the regime. The SR absorption rate of the floor under the SC collector was measured by using a constraint that influences the system's performance efficiency. Ismaeel et al. [10] presented a hybrid thermal material for thermal energy storage (TES). This substance is simple as well as capable of absorbing and storing the SE, thus enhancing performance and extending the time of working. Khidhir and Atrooshi [11] included the overall variation in thermal radiation within the conversion region and the resulting increase in temperature in response to hourly changes in ambient temperature. Sadiq [12] and Sadiq et al. [13] proposed compressed air energy storage (CAES) systems, such as biomass, low temperature geothermal, solar and waste heat, to reduce CO_2 emissions. Osama and Shyaa [14] and Sirror [15] studied a review paper about the effect of

windcatcher and SC in passive cooling.

Al-Azawiey et al. [16] investigated the influence of collector height on airflow temperature and mass flow rate, demonstrating that enhanced HT directly improves system performance. Al-Azawiey and Hassan [17] enhanced the collector energy transformation efficacy and used a heat storage medium to extend its operating time. They used 6 ground substances that are obtainable in Malaysia, studying their solar thermal conversion and thermal storage capabilities experimentally and numerically.

The novelty of this research lies in integrating ribbed and dual aluminum rib configurations into SC collectors to enhance the HT and airflow performance. In contrast to conventional flat-plate designs, the incorporation of aluminum ribs and a secondary AP promotes turbulence, disrupts thermal boundary layers, and enlarges the effective heat exchange surface. These modifications significantly improve the rate of mass flow as well as the temperature of the outlet air. Moreover, three-dimensional simulation of computational fluid dynamics (CFD) and practical validation are employed in this study, which guarantees reliable findings and presents an expediency of natural ventilation systems development together with low cost to create a natural ventilation system to enhance indoor comfort.

2. SYSTEM DESCRIPTION MODEL

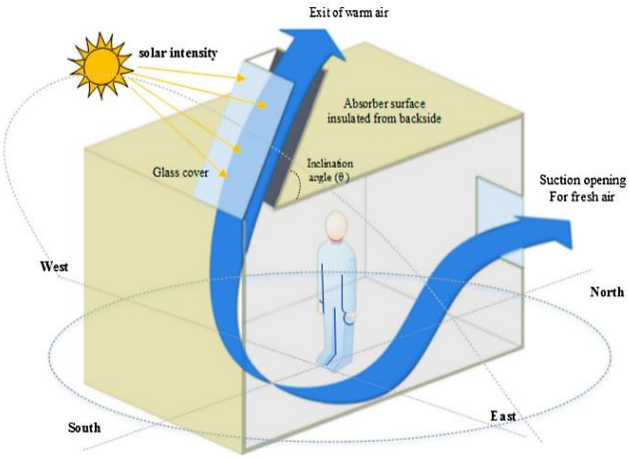

(a)

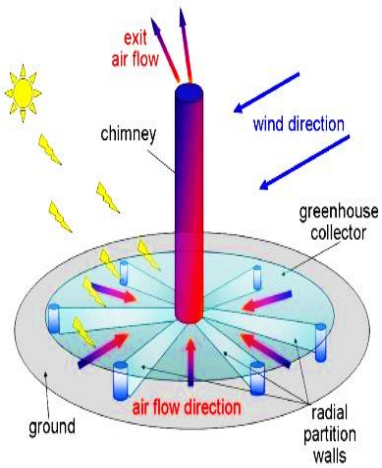

(b)

Figure 1. (a) Diagram of the ventilation flow of a single room with a solar chimney (SC) model [18]; (b) the SC power plant [19]

Figure 1 shows how SC works as a ventilation or as a power plant [18, 19]. In this system, SE is first converted into thermal energy and subsequently transformed into kinetic energy. In this system, air is heated via SR beneath a circular glass roof, which also heats the AP. At the center of the roof, an inclined or vertical chimney is installed with large air inlets. Also, the collector comprises a cover made of glass or transparent plastic roof, through which the SR penetrates, heating the air. This roof traps the heat that is re-radiating from floor and transmits SR with shorter wavelengths while capturing SR from the floor. Also, the collector floor is consequently heated, thereby heating the air flowing within the collector. Aluminum, which has good physical properties, is used as the material for the floor. In this work, an aluminum plate floor that was painted black to enhance its absorptivity generates a heat source that heats the collector as well as increases the flowing air temperature. Additionally, the collector, having its streamlined design, serves as a heat engine together with the chimney. Furthermore, the discrepancy of pressure at the chimney ends, the discrepancy of density between the hot air in the collector and the cold air outside the collector, and the streamlined shape all raise the kinetic energy of air exiting the chimney. Direct sunlight is not needed for SCs to be effective; they can utilize diffuse radiation and thus function even in cloudy conditions, ensuring stable operation. They are also protected from intermittent winds, thus being a satisfactory development in this field.

3. NUMERICAL ANALYSIS

CFD is used to study the performance of fluid systems prior to manufacturing. In this work, CFD is used to simulate the flow of air throughout a solar collector, thereby enabling the impact analysis of adding ribs through ANSYS Fluent, advanced software for the flow of fluid modeling HT in complex geometries. The finite volume technique was employed for solving the equations of continuity, momentum [20], and energy through a steady-state analysis. Air was used as the working fluid to simulate the real-life fluid flow, and it was modeled as a perfect gas. And the buoyancy model was used to enhance simulation accuracy, and gravity was set to (-g) in the (y) direction. A reference pressure of 1 standard atmosphere (atm) was used to ensure reliable findings [11].

3.1 Creating geometric models

SolidWorks was employed to generate the geometric model of the system (see Figure 2), which was subsequently discretized using a tetrahedral mesh. A tetrahedral mesh is a three-dimensional discretization technique in which each element takes the form of a tetrahedron, a polyhedron with four triangular faces. Such a mesh is especially beneficial in finite element analysis (FEA), CFD, and other numerical simulations due to the flexibility of dealing with very complex and irregular geometry. Tetrahedral meshes are also more capable of fitting irregularly shaped surfaces and curved boundaries with greater accuracy than organized meshes (which are bounded by regular structures), meaning that high-fidelity simulations in such areas are more likely to occur. In addition, tetrahedral elements facilitate automatic meshing in computer-aided design (CAD) and simulation programs, saving time spent on manual mesh generation. Tetrahedral elements are also favored in early design studies and design optimization investigations.

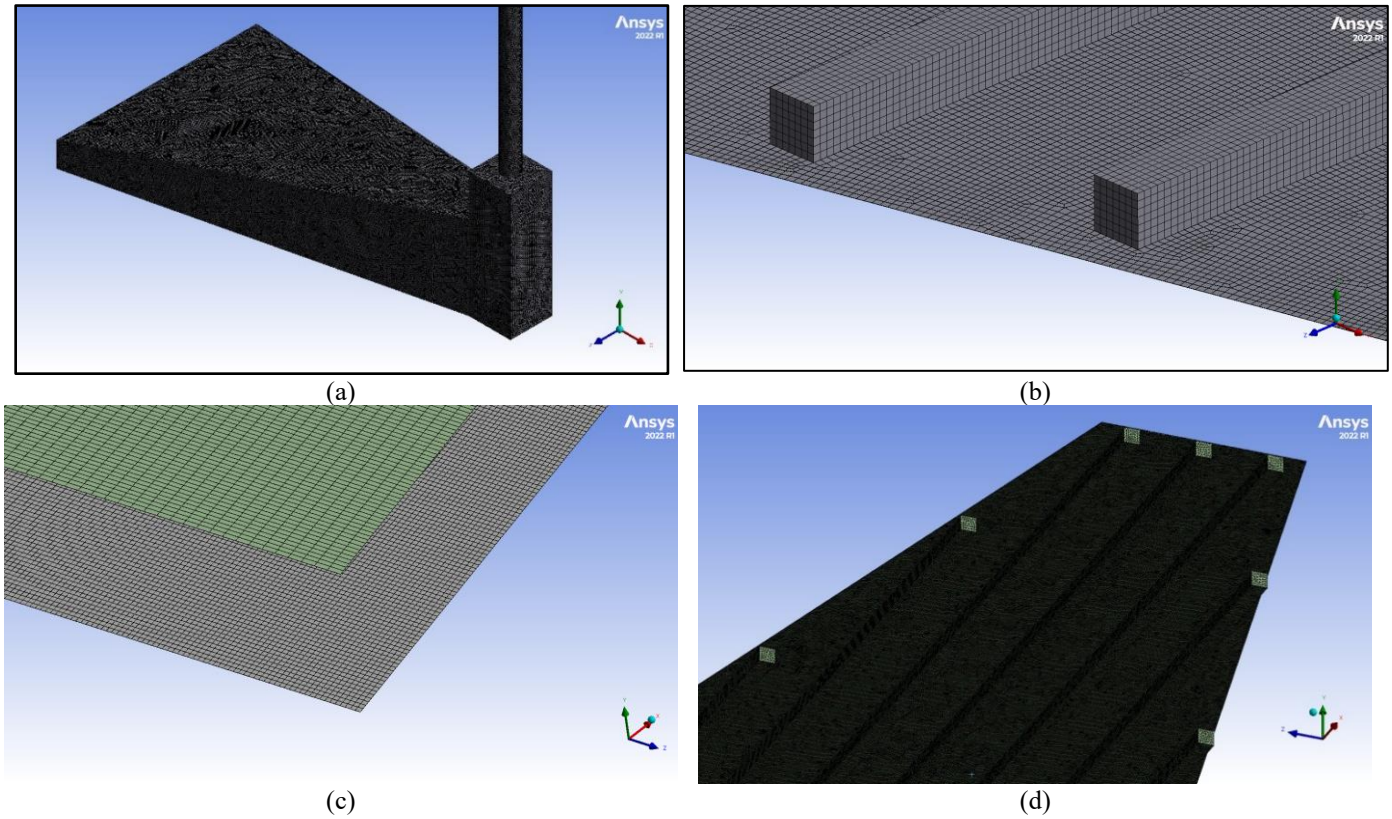

Figure 2. (a) Mesh of the SC model, (b) mesh of the ribs at the absorber plate (AP), (c) mesh of the insert AP, and (d) longitudinal ribs on the insert AP

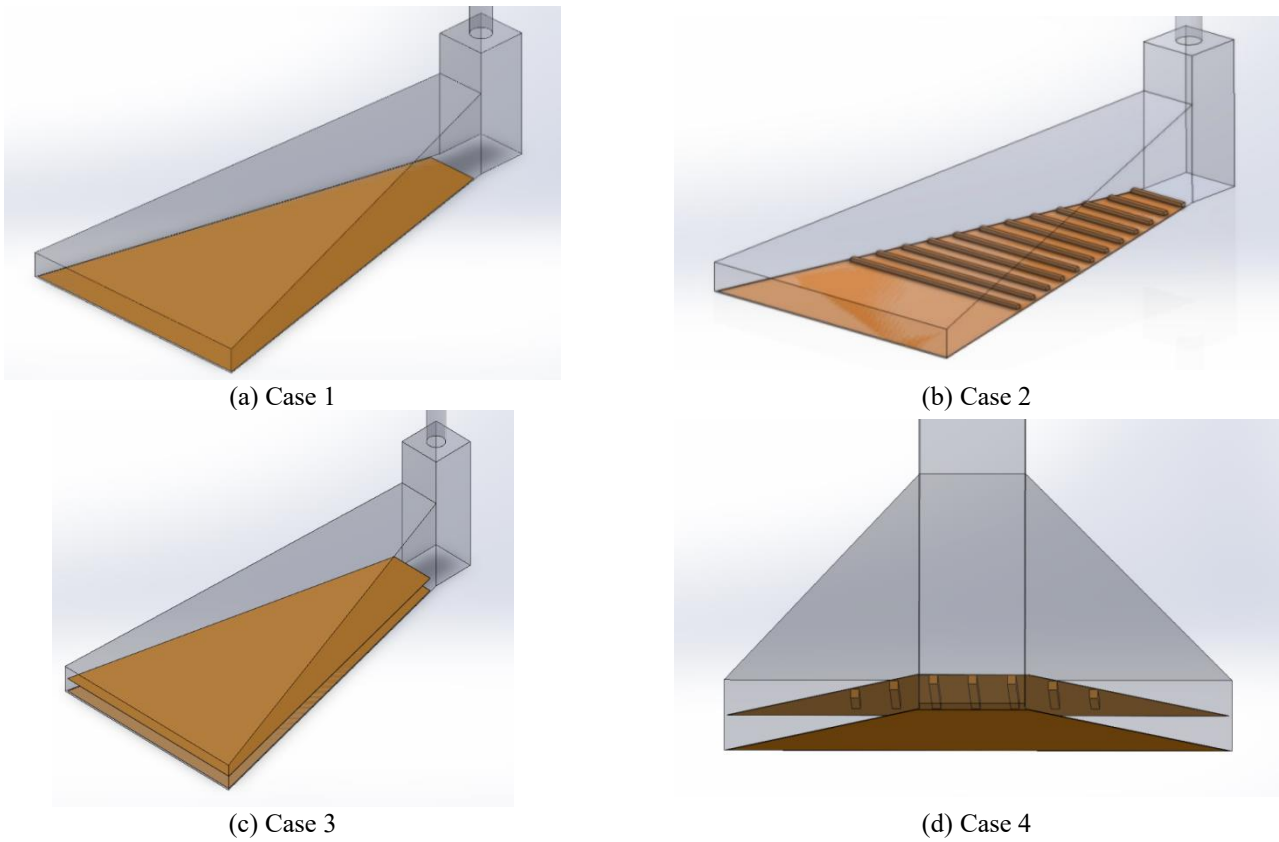

Figure 3. SolidWorks software program for solar chimney case studies

The meshing approach adopted in this study is particularly effective for the geometries and flow fields that require fine resolution in specific regions of the computational domain. A mesh tetrahedron type was employed to ensure higher accuracy and numerical stability. Table 1 summarizes the mesh characteristics, while the thermo-physical properties of the aluminum plate and air were obtained directly from the ANSYS material database [21].

Table 1. Mesh details

Parameter	Description
Collector diameter (m)	200 m
Collector height (m)	0.15 m
Collector width (m)	1.20 m
Canopy angles	30°
No. of ribs	12 for case 2, 7 for case 4
Mesh type for plate	Multi-zone structured
Mesh type for air	Tetrahedron mesh
Minimum cell size near walls	0.2
Growth ratio	1.2

The 3D, steady-state conservation equations of mass, momentum, and energy are now explicitly stated and referenced. Air is modeled as an ideal gas under the Boussinesq approximation, with buoyancy activated via gravity in the vertical direction.

The turbulence model is clearly specified by using the k-ε model consistent with the buoyancy correction. The experimental absorber coating included surface emissivity and absorptivity values.

The resulting mesh configurations for the four considered case studies are illustrated in Table 1. SolidWorks was utilized to develop geometric models for the four SC case studies. In Case 1, a flat aluminum AP represented the baseline reference. Case 2 featured 12 flat aluminum ribs attached to the AP to generate turbulence and disturb the thermal boundary layer. Case 3 added a secondary AP positioned at the mid-plane of the collector, dividing the airflow into two channels. In Case 4, longitudinal flat aluminum ribs were incorporated on the secondary plate to intensify localized mixing and improve heat absorption. This modeling approach can be seen in Figure 3, ensuring accurate CFD analysis and enabling consistent comparison of thermal and flow performance across the four configurations.

3.2 Governing equations

These equations for simulation and the assumptions for the 3-D steady-state model are presented here. And the continuity formula can be expressed as [22]:

$$\frac{\partial}{\partial z}(\rho u) + \frac{1}{r}\frac{\partial}{\partial r}(\rho v) = 0 \tag{1}$$

$$\begin{aligned}\frac{\partial}{\partial z}(\rho u u) + \frac{1}{r}\frac{\partial}{\partial r}(\rho u v) = {} & \frac{\partial p}{\partial z} + (\rho - \rho_0) \\ & + 2\frac{\partial}{\partial z}\left[(\mu + \mu_t)\frac{\partial u}{\partial z}\right] \\ & + \frac{1}{r}\frac{\partial}{\partial r}(\mu + \mu_t) r \left(\frac{\partial u}{\partial z} + \frac{\partial v}{\partial r}\right)\end{aligned} \tag{2}$$

$$\begin{aligned}\frac{\partial}{\partial z}(uT) + \frac{1}{r}\frac{\partial}{\partial r}(ruT) = {} & \frac{1}{\rho} + \frac{\partial}{\partial z}\left[\left(\frac{\mu}{Pr} + \frac{\mu_t}{\sigma_t}\right)\frac{\partial T}{\partial z}\right] \\ & + \frac{1}{\rho r}\frac{\partial}{\partial r}\left[\left(\frac{\mu}{Pr} + \frac{\mu_t}{\sigma_t}\right) r \frac{\partial T}{\partial z}\right]\end{aligned} \tag{3}$$

The thermal expansion coefficient (β) is calculated by Eq. (1), assuming small temperature changes.

$$\beta = \frac{1}{\rho}\left(\frac{\partial \rho}{\partial T}\right)_P \approx \frac{1}{\rho}\left(\frac{\rho_o - \rho}{T_o - T}\right) \tag{4}$$

The density of air (ρ) into a flow can be mathematically calculated by this equation:

$$(\rho - \rho_o) \approx \rho_o \beta (T - T_o) \tag{5}$$

3.3 Boundary operating condition and setup setting

To ensure the mass and momentum are conserved across the domain, the natural buoyancy-driven inflow and outflow of air under solar heating were simulated. And the AP, which was produced from the aluminum, was thermally characterized with an emissivity of 0.95 and an absorptivity of 0.9, reflecting its high capability to absorb incident SR and re-radiate energy as heat. The black-painted aluminum surface used in the experimental setup realistically models radiative and convection heat transfer (CHT) interactions within the collector. And the thermo-physical properties of materials considered in the model, including air, glass, steel, wood, and insulation, are summarized in Table 2. The complete set of applied boundary conditions is illustrated in Figure 4, which provides a schematic illustration of the computational domain, comprising inlet and outlet zones, heated AP, and surrounding collectors and chimney structure. Together, these conditions ensure that the numerical model accurately reproduces the thermal as well as the fluid dynamic environment of the experimental SC system.

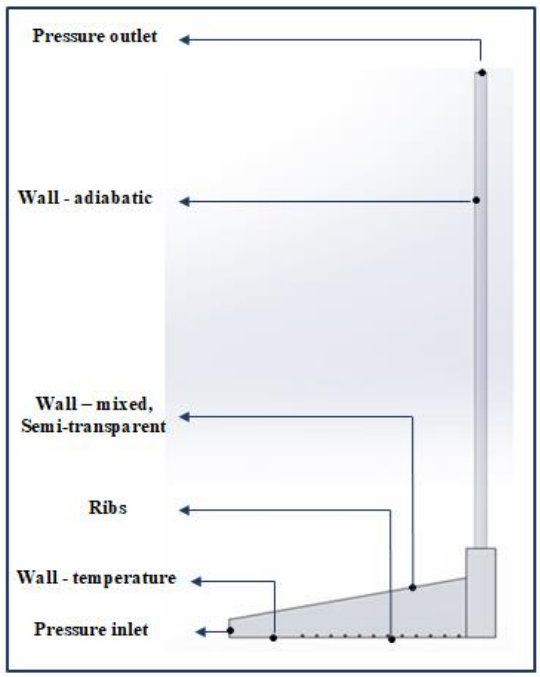

Figure 4. The boundary conditions of computational domain

Table 2. Thermal-physical properties of the material

Properties	Air	Glass	Aluminum	Wood	Insulation
Density (kg/m^3)	1.18	2220	2689.8	700	10
CP (specific heat) (J/kg/K)	1006.43	830	0.219	2310	830
Thermal conductivity (w/m.K)	0.0242	1.15	238.659	0.173	0.1
Viscosity (kg/m.s)	1.7894E-5	-	-	-	-
Coefficient of thermal expansion (1/K)	0.00335	-	-	-	-

4. EXPERIMENTAL SETUP

The experimental model was constructed at the Mechanical Engineering Department, College of Engineering, Mustansiriyah University, with the objective of evaluating the thermal and flow performance of an SC system. The construction had two major features: a solar collector and a vertical chimney. The collector had a total size of 2.0 m long, 1.2 m wide and 0.15 m high, and, therefore, it offered some compact but representative geometry, which was suitable to be tested in an experiment. The chimney installed on the outlet of the collector had a height of 4.0 m and a diameter of 0.1 m. These dimensions were chosen to provide enough draft due to buoyancy and provide a structure that is not too complex. In Figure 5, the SC was designed deterministically, as far as its geometric constituents are concerned. A hard wireframe was used to make the collector body stable and easier to assemble. The frame was then covered with a sheet of clear nylon, which was used as the glazing material to ensure that the SR reached inside the frame, but little heat was lost to the environment through convection. The external surfaces of the collector were covered further with wooden panels to provide extra thermal insulation protection and structural support. These types of designs guaranteed that the system was able to trap and store solar heat, and this was simulating the real conditions of operations when exposure was outdoors.

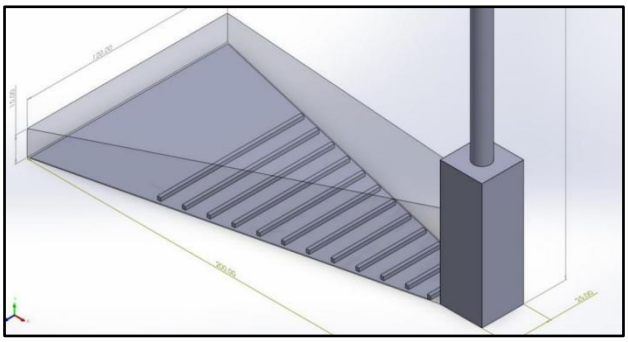

Figure 5. Dimension of the absorber aluminium plate

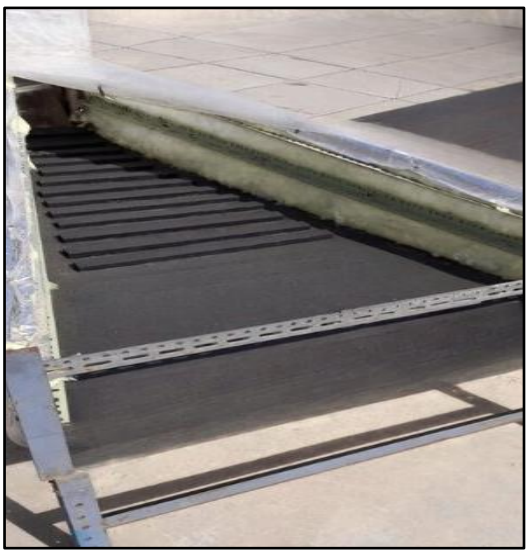

Figure 6. Plate of the test section with 12 flat ribs along the absorber aluminium plate

A critical modification in this design was the integration of twelve flat aluminum ribs onto the AP. These ribs in an experimental test rig with a rectangular cross-section were mounted longitudinally along the surface of the absorber to intensify HT between the heated plate and the flowing air. The ribs enhanced turbulence within the collector channel, thereby disrupting the thermal boundary layer and increasing the effective heat exchange surface area. As a result, the temperature of the airflow was significantly elevated, while the AP maintained more uniform surface temperatures. Detailed specifications of the AP, including its material properties, rib geometry, and surface treatment, are presented in the following section (Figure 6).

4.1 Data processing

The velocity, inlet and outlet temperatures, and solar collector's surface temperatures are measured experimentally and used to compute the performance indicator (PI) and efficiency (η) [23]. And the subsequent assumptions were regarded for developing the mathematical modeling for SC:

1) The steady-state performance of the solar chimney power plant (SCPP) is examined.
2) The air behaved like an ideal gas.
3) The system's airflow is induced by natural convection (NC).
4) Collector's flow is supposed to be generated between 2 parallel plates.
5) Airflow of the system is caused by the buoyancy force.
6) Solar collectors are isolated.

The details of the HT equations are presented in Figure 7 [24].

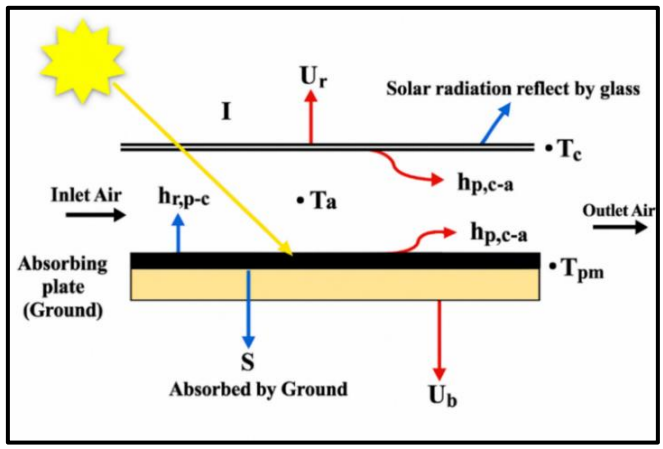

Figure 7. Schematic of the heat transfer (HT) in the solar collector

Glass cover:

$$U_t\,(T_a - T_c\,) + h_r\,(T_p - T_c) + h_1(T_f + T_c) = 0 \qquad (6)$$

Airflow of collector:

$$h_1(T_c - T_f) + h_2(T_p - T_f) = q_u \qquad (7)$$

Absorber plate:

$$S + h_2(T_f - T_p) + h_r(T_c - T_P) = 0 \qquad (8)$$

The heat loss between the glass cover and the AP because of radiation is mentioned as a maximum Heat Loss Coefficient (HLC). The CHT between the inside of the collector and both

the AP and the glass cover plays a significant role in the system's thermal performance. The HF absorbed via AP is obtained as [24]:

$$S = \alpha\tau I_T \tag{9}$$

The heat transfer coefficient (HTC) via radiation between the AP and the glass cover is:

$$h_r = \frac{\sigma(T_c+T_p)(T_c^2+T_p^2)}{(\frac{1}{\varepsilon_p}+\frac{1}{\varepsilon_c}-1)} \tag{10}$$

Considering the forced convection HTC coefficient between AP and glass cover, the collector storage walls and solar air heaters need to be evaluated. Kay's correlation can be used to calculate the coefficient for air. This method, which is considered a reliable calculation approach, involves heating one side and insulating the other Al-Azawiey et al. [16].

$$Nu = 0.0158Re^{0.8} \tag{11}$$

$$h_1 = h_2 = \frac{N_u K}{D_H} \tag{12}$$

An empirical equation is used to calculate the overall top HLC, as described by Al-Azawiey and Hassan [17]:

$$U_t = \left\{\frac{N}{\frac{c}{T_p}\left[\frac{(T_p-T_a)}{(N-f)}\right]^e} + \frac{1}{h_w}\right\}^{-1} \frac{\sigma\left(T_p^2+T_a^2\right)\left(T_p+T_a\right)}{\left(\varepsilon_p + 0.00591\, N\, h_w\right\}^{-1} + \left[\frac{2N+f-1+0.133\varepsilon_p}{\varepsilon_c}\right]} \tag{13}$$

$$h_w = 2.8 + 3\ V_w \tag{14}$$

where,

- V_w = Wind speed m/s
- N = Number of glass covers

$$f = (1 + 0.089h_w - 0.1166h_w\varepsilon p)\ (1 + 0.07866\ N) \tag{15}$$

$$c = 520\ (1 - 0.000051\ \beta^2) \tag{16}$$

For $0^\circ < \beta < 70^\circ$, For $70^\circ < \beta < 90^\circ, \beta = 70^\circ$

where, β is the tilt of collector (Degrees).

The Back-Loss Coefficient (Ub) is:

$$U_b = \frac{K}{\delta} \tag{17}$$

where,

- K: The insulator thermal conductivity
- δ: The thickness

The overall HLC (UL) of collectors is given by [9]:

$$U_L = (U_b + U_t)\ (h_1h_2 + h_1h_{r,p\text{-}c} + h_2h_{r,p\text{-}c}) + U_bU_t\ (h_1 + h_2)\ h_1h_{r,p\text{-}c} + h_2U_t + h_2h_{r,p\text{-}c} + h_1h_2 \tag{18}$$

where,

- h_1: The HTC by convection between the glass cover and airflow
- h_2: The HTC by convection between AP and airflow

h_1 and h_2 can be presumed as:

$$h_1\ or\ h_2 = N_u\ \frac{k}{D_h} \tag{19}$$

The following equation was used to derive the quantity of heat that was gained via the collector's hot air:

$$q_u = \frac{C_p\dot{m}}{A_c}(T_o - T_a) \tag{20}$$

where, $\dot{m}$ represents the rate of hot air mass flow in SC or in collector and can be calculated as:

$$\dot{m} = \rho V_{ch} A \tag{21}$$

where,

- ρ: The density of air at the collector outlet (kg/m^3)
- V: The hot air velocity at the collector outlet (m/sec)
- A: Cross-sectional area of the chimney (m^2)

The PI for the suggested model is computed as a product of the rate of mass flow ($\dot{m}$) through the system and the air temperature gain in the regime (ΔT) [25, 26].

$$\Delta T = T_{air.out} - T_{amb} \tag{22}$$

$$PI = \dot{m} \cdot \Delta T \tag{23}$$

The solar collector efficacy is calculated as the beneficial heat gain of hot air in the collector, as shown in this equation:

$$\dot{\eta}_c = \frac{q_u}{I_T} \tag{24}$$

Twelve K-type thermocouples were integrated into the test rig. Two were strategically placed at the solar collector's inlet and outlet, while the remaining thermocouples were evenly distributed along the absorbing plate and cover, spaced 250 mm apart. Thermocouples (Type K) offer a wide range of temperature measurements (-100–1300°C) with a commendable accuracy of ±2.2°C or ±0.75% (standard). Notably, the entrance region remained rib-free for 0.75 m, as used by Chabane. All K-type thermocouples were calibrated against a standard mercury thermometer prior to experimentation. Calibration was performed in a controlled temperature bath covering the expected operating range. The efficacy of collectors is primarily affected by two key factors ($\dot{m}$ × ΔT). To enhance these factors, four case studies were employed. The first case was the addition of 12 flat aluminum ribs having a rectangular cross-section on the aluminum AP. The second case was adding the AP in the middle, parallel to the ground AP. Finally, longitudinal 12 flat aluminum ribs having a rectangular cross-section were added, thereby improving the HT along the collector. The primary objective of such an experimental study is to carry out a thorough analysis comparing the enhancement effects of the AP upon the HT from the plate to the air, as well as upon the difference in temperature.

5. RESULTS AND DISCUSSION

5.1 Validation

The Case 1 (baseline flat AP without ribs) outcomes were

confirmed via the comparison of the simulated thermal performance with the investigational results reported by Al-Azawiey et al. [16]. The validation was conducted over an eight-hour operating period (08:00–15:00), which encompassed the morning increase in SR, thereby representing the full daily variation in collector behavior. As shown in Figure 8, the predicted temperature of the outlet air and the rate of mass flow exhibited a close correlation with the reference results, validating the CFD model's reliability in capturing the diurnal performance of the SC. Both datasets displayed similar trends, with temperature and airflow gradually increasing in the morning as SR intensified, reaching peak values around midday, and subsequently decreasing in the afternoon. The alignment between the present simulation and the benchmark results demonstrates that the governing equations, boundary conditions, and material property assumptions employed in this study are appropriate.

5.2 Numerical result

The simulated temperature spreading within the solar collector for different design configurations is presented in Figure 8, clearly illustrating the influence of ribs on the HT process. Figure 9 represents the baseline case without any internal enhancements, where the gradient of temperature between the inlet and the outlet air is relatively small, indicating limited heat absorption from the absorb plate to the airflow.

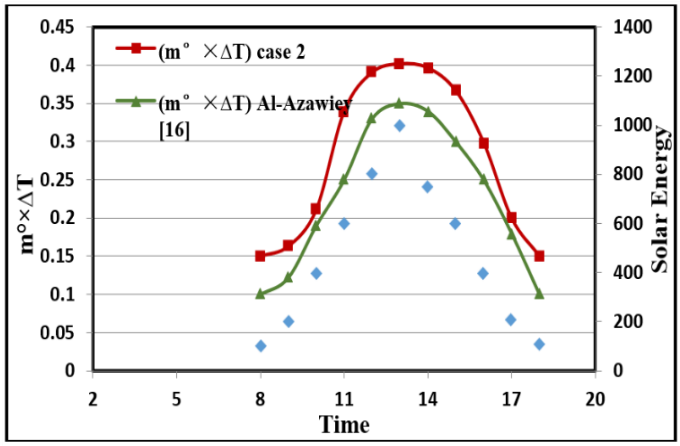

Figure 8. Validation between this study and Al-Azawiey et al. [16]

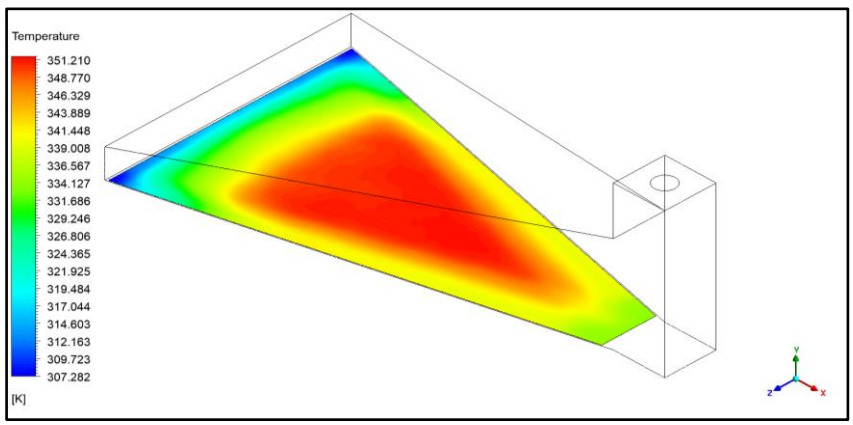

Figure 9. Temperature contour of the AP

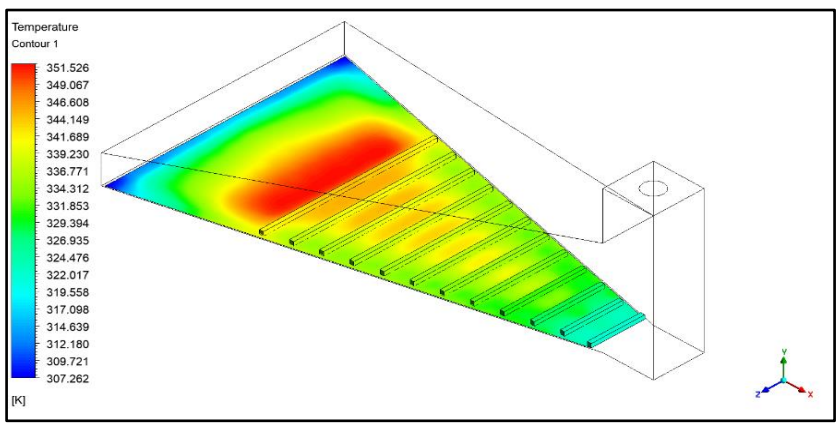

Figure 10. Temperature contour of the AP

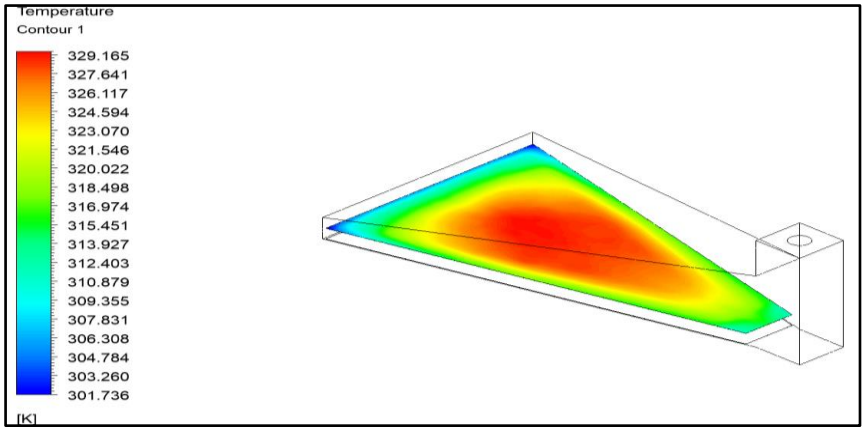

Figure 11. Temperature contour of the eddy AP temperature

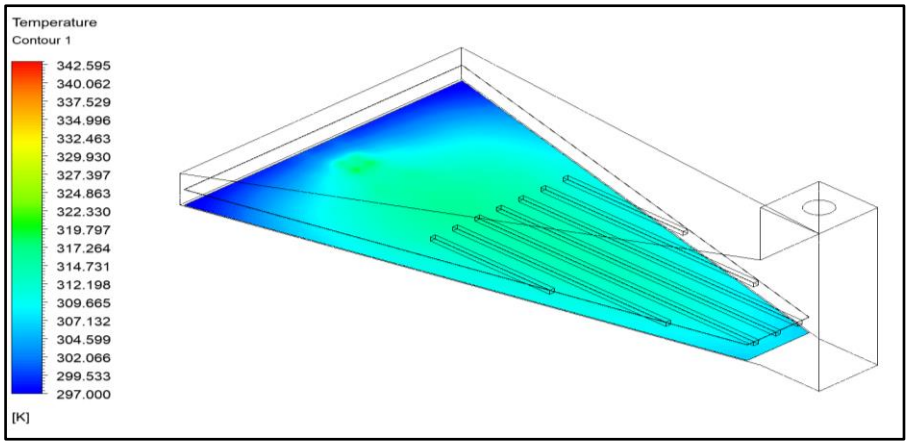

Figure 12. Contour of the eddy absorb plate temperature

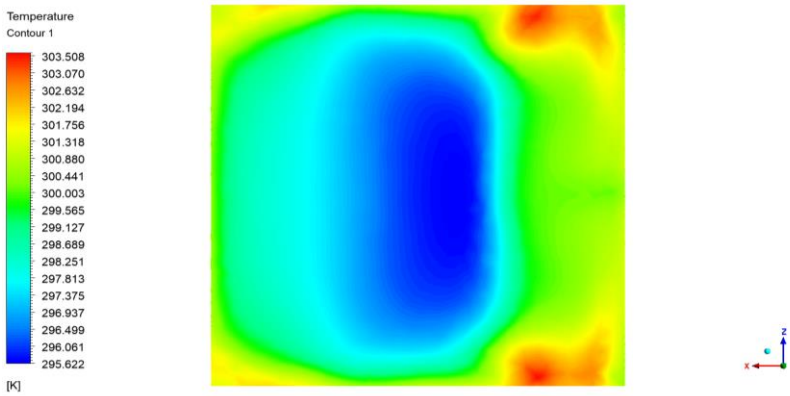

(a) Case 2

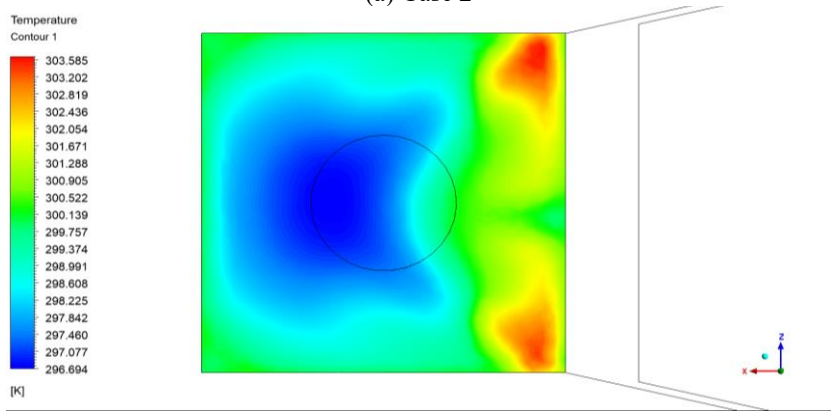

(b) Case 4

Figure 13. Contour of the difference of temperature between the collector inlet and outlet of the (a) Case 2 and (b) Case 4

In contrast, Case 2 (Figure 10) illustrates the configurations of different ribs. This improvement is attributed to the ability of the ribs to induce localized turbulence, disrupting the thermal boundary layer, and allowing for more effective energy transfer from the plate to the airflow. Monitoring AP temperature profiles is therefore essential, as excessively high plate temperatures may signal inefficient energy extraction, while uniformly elevated outlet air temperatures confirm successful enhancement of HT. These observations underscore the structural modifications, such as the rib integration, can be an effective, low-cost strategy for improving the SC collector performance, especially under the NC conditions. Figure 11 illustrates the insertion of double AP to enhance the temperature difference and maximize the heat transfer to the air. The existence of the eddy plate ensured that the total amount of surface area used to exchange the heat was maximized and further spreading of air was facilitated, which augmented the heat absorption capacity of the system. Case 4 (Figure 12) was constructed because of this structure and gave flat aluminum ribs to the eddy AP surface. These ribs were flow disruptors that created regulated turbulence in the stream of air. The turbulence created a good opportunity to penetrate the thermal boundary-layer, which usually develops on the HT surfaces, enhancing the CHT between the moving fluid and plate. This process brought a faster and better HT between the absorbing and the airflow. Therefore, the ribbed eddy plate design recorded significantly higher air temperatures than the other arrangements, at the peak outshine conditions, especially at around 1:00 p.m., where the solar intensity was at its peak, and the flow rates due to buoyancy were at their highest rate.

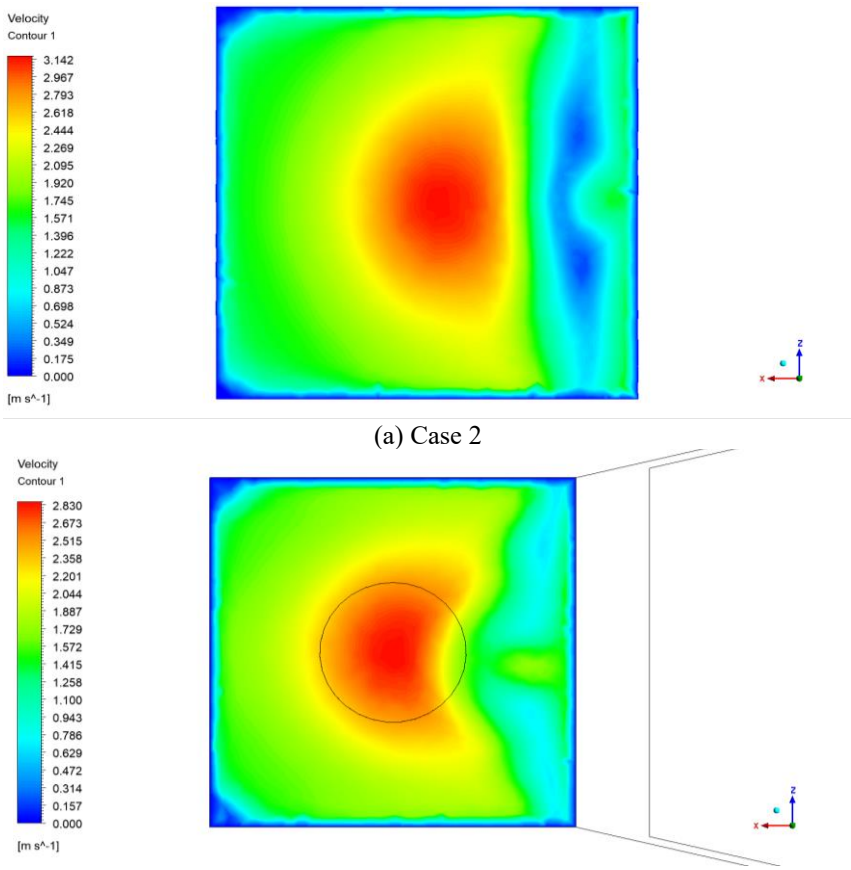

Figure 14. Contour of the air velocity in the collector with ribs (a) Case 2 and (b) Case 4

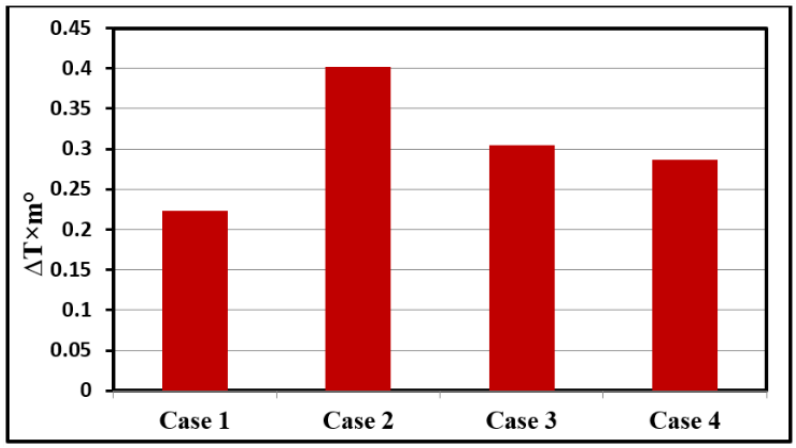

Figure 15. Behavior of the four case studies (mass flow rate ($\dot{m}$) × temperature difference (ΔT))

The exhaustive numerical research in four case studies indicated that Cases 2 and 4 recorded the highest gain in HT between the AP and the solar collector airflow. In Case 2, the enhanced thermal performance was mostly explained by a simultaneous increase of the mass flow rate and the temperature difference, which suggested that the introduction of the flat aluminum ribs was efficient in breaking the thermal boundary layer, increasing stronger turbulence and enhancing CHT, keeping the high airflow rates. This two-fold enhancement not only aids in the increased transfer of energy in the warmed surface of the absorbent to the flowing air but also helps towards an additional even distribution of temperature in the flow way. On the other hand, in Case 4, the improvement that took place was mostly because of a significant rise in temperature difference as opposed to a relative rise in the rate of mass flow. The longitudinal rib arrangement here increased localized mixing and heat absorption that resulted in the increase in air temperature, but since the mass flow in the generated flow was overall constrained by the induced resistance to flow a little. These trends can be well illustrated by Figure 13, which shows the unique thermal and velocity field pattern between the two layouts and the trade-off existing between the flow rate and temperature gain in optimizing rib geometry as used in the SC applications. Gradual acceleration results in passing air through a solar collector due to the unremitting absorption of the air through the AP, leading to the heating of the air that lowers its density. This acceleration due to buoyancy is more visible as the air nears the chimney inlet, within which a degree of sudden increase of velocity is noticed in both Case 2 and Case 4 (Figure 14). The sudden increase at this point is explained by the narrowing and increased pressure difference between the bottom of chimney and the outlet of collector, causing the hot air to ascend with more velocity. The effect of ribs on the floor of the AP is to change dramatically this velocity behavior; the ribs introduce turbulence locally in the smooth laminar boundary layer and improve the ability to mix the airflow. In addition to disruptions in the otherwise stable velocity profile, this turbulence amplifies the CHT between the AP and the moving air. This causes the collector velocity distribution to be more non-uniform with jets of higher velocity being in the downstream of the ribs and eventually leads to better thermal performance than the smooth, rib-free design.

Figure 15 represents a relative comparison of the numerically predicted value with the experimental value of the key performance parameters of the SC regime that are the temperature of AP, the temperature of airflow and air velocity in the inlet of the chimney, which have all been obtained under the same operating conditions to provide a fair comparison.

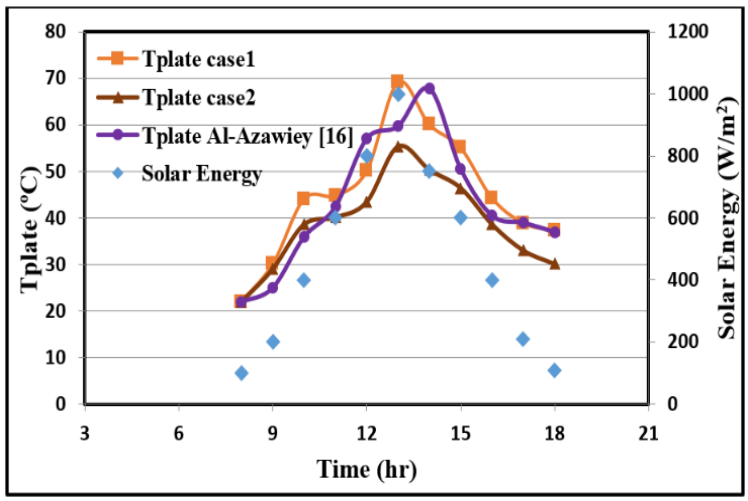

Figure 16. Experimental result for mass flow rate ($\dot{m}$) × temperature difference (ΔT)

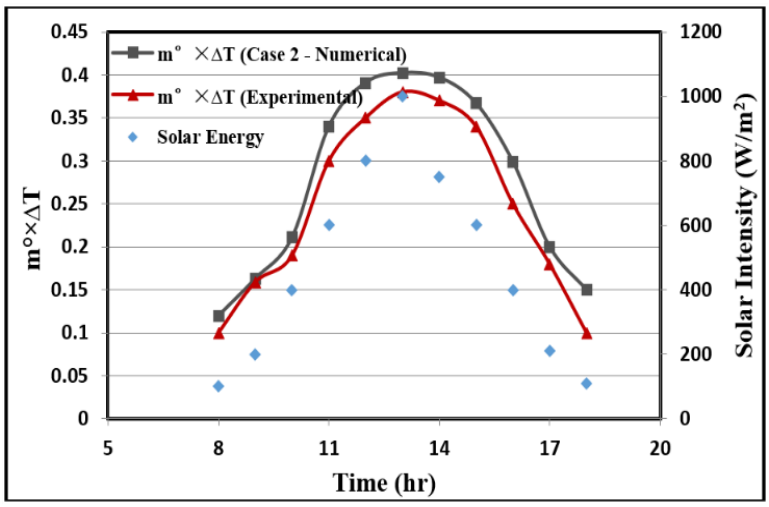

Figure 17. Comparisons between experimental and numerical results

5.3 Experimental result

The approaches show strong consistency, with CFD simulations generally predicting slightly higher values than those recorded experimentally. Both the numerical results, the findings of Al-Azawiey et al. [16], and the experimental data confirm a clear linear relationship between the collector component temperatures and the measured solar Intensity (SI), demonstrating that an increase in SR directly leads to a proportional rise in temperature. Moreover, Figure 16 illustrates that the AP temperature increases with solar intensity for all the case studies, while Case 2 recorded comparatively lower temperatures due to its enhanced PI, reflecting improved HT from the plate to the airflow.

The observed differences can be attributed to inevitable factors such as minor experimental setup inaccuracies, sensor calibration limitations, and variations in outdoor environmental conditions. As shown in Figure 17, the structural modifications significantly influenced performance, with the results compared using the combined thermal performance parameter ($\dot{m} \times \Delta T$), where $\dot{m}$ represents the mass flow rate and ΔT the temperature rise. The numerical simulations clearly highlight the positive effect of adding ribs to the AP in the SC system. Both experimental and numerical approaches reveal a consistent trend, confirming that ribbed configurations deliver superior performance compared to the baseline.

6. CONCLUSION AND FUTURE WORK

The best-performing configuration (Case 2) is justified using numerical values of efficiency, temperature rise (ΔT), and mass flow rate ($\dot{m}$). Comparative statements between configurations are explicitly tied to PIs ($\dot{m} \times \Delta T$) rather than subjective wording. Among the four examined configurations, Case 2 demonstrated the best overall efficiency, reaching 17.6% at 1:00 p.m., which corresponds to nearly a 60% improvement compared to the baseline flat AP (Case 1). While Case 3 achieved the largest temperature difference, with an increase of approximately 40% over the baseline, its efficiency was constrained by a reduced mass flow rate. Similarly, Case 4 delivered about a 45% enhancement in ΔT, but this gain came at the expense of slightly lower airflow compared with Case 2. These outcomes underscore that the efficiency of SC collectors is determined by:

1. Performance improvements are now expressed using measured enhancement ranges rather than qualitative descriptors.
2. The best-performing configuration (Case 2) is justified using numerical values of efficiency, temperature rise (ΔT), and mass flow rate ($\dot{m}$).
3. Comparative statements between configurations are explicitly tied to PIs ($\dot{m} \times \Delta T$) rather than subjective wording.

Overall, the study confirms that integrating ribs into APs offers a low-cost, scalable, and effective approach to improving natural ventilation and renewable energy performance in SC systems. The strong agreement between CFD simulations and experimental measurements further validates the reliability of the numerical model, establishing a solid foundation for future optimization. Prospective research could focus on alternative rib geometries, hybrid absorber configurations, and the incorporation of thermal storage materials to further extend operating time and enhance efficiency.

Future directions:

- Parametric optimization of rib geometry (height, spacing, thickness, and shape) to balance HT enhancement against pressure drop.
- Hybrid systems integration, including PCMs or thermal energy storage layers beneath the AP.
- Investigate alternative rib configurations.

ACKNOWLEDGMENT

The authors thank the University of Mustansiriyah (www.uomustansiriyah.edu.iq), Baghdad, Iraq, for its support in the current research.

REFERENCES

[1] Setareh, M. (2021). Comprehensive mathematical study on solar chimney powerplant. Renewable Energy, 175: 470-485. https://doi.org/10.1016/j.renene.2021.05.017

[2] Abdelsalam, E., Kafiah, F., Almomani, F., Zawati, H., Muheidat, A., Yaseen, L.B. (2023). The potential of employing a novel hybrid solar chimney power plant in the Arabian Gulf: A case study. Case Studies in Thermal Engineering, 51: 103532. https://doi.org/10.1016/j.csite.2023.103532

[3] Yue, S.K., Ge, Z., Xu, J., Xie, J.B., Xie, Z.Y., Zhang, S.Y., Li, J. (2023). Analysis of the ventilation performance of a solar chimney coupled to an outdoor wind and indoor heat source. Applied Sciences, 13(4): 2585. https://doi.org/10.3390/app13042585

[4] Albaldawi, R.A., Shyaa, A.K., Nuri, H.S. (2014). Heat storage enhanced in solar chimney power plant model by using PCM material. Proceedings of the ASME 2014 Power Conference, Baltimore, Maryland. V002T09A001. https://doi.org/10.1115/POWER2014-32005

[5] Nie, J., Xu, J., Su, H., Gao, H., Jia, J., Guo, T. (2024). Optimization of characteristic parameters of rectangular solar chimney adapted to agricultural greenhouses. Case Studies in Thermal Engineering, 54: 03971. https://doi.org/10.1016/j.csite.2024.103971

[6] Ren, X.H., Wang, P.L., Zhang, C.X., Song, Y.J., Shang, J., Wang, L., Zhao, F.Y. (2024). Heat removal and ventilation limitations of the solar chimney attached with a built enclosure: Correlations of thermal Rayleigh numbers, port arrangements and discrete heating elements. Renewable Energy, 221: 19782. https://doi.org/10.1016/j.renene.2023.119782

[7] Chikere, A.O., Al-Kayiem, H.H., Karim, Z.A.A. (2011). Review on the enhancement techniques and introduction of an alternate enhancement technique of solar chimney power plant. Journal of Applied Sciences, 11(11): 1877-1884. https://doi.org/10.3923/jas.2011.1877.1884

[8] Dos Santos Bernardes, M.A., Von Backström, T.W., Kröger, D.G. (2009). Analysis of some available heat transfer coefficients applicable to solar chimney power plant collectors. Solar Energy, 83(2): 264-275. https://doi.org/10.1016/j.solener.2008.07.019

[9] Buğutekin, A. (2012). An experimental investigation of the effect of periphery height and ground temperature

changes on the solar chimney system. Isi Bilimi ve Teknigi Dergisi–Journal of Thermal Science and Technology, 32: 51-58.
[10] Ismaeel, A.A., Al-Kayeim, H.H., Baheta, A.T., Aurybi, M.A. (2016). Comparative critique of thermal energy storage technique in solar chimney power plants. International Energy Journal, 16(1): 11-24.
[11] Khidhir, D.K., Atrooshi, S.A. (2020). Investigation of thermal concentration effect in a modified solar chimney. Solar Energy, 206: 799-815. https://doi.org/10.1016/j.solener.2020.06.011
[12] Sadiq, G.A. (2020). Development of rotary Wankel devices for power generation. IOP Conference Series: Materials Science and Engineering, 870(1): 012169. https://doi.org/10.1088/1757-899X/870/1/012169
[13] Sadiq, G.A., Tozer, G.M., Mahmoud, S.M., Al-Dadah, R.K. (2016). Numerical investigation of the two stage Wankel expander performance. In 2016 International Conference for Students on Applied Engineering (ICSAE), Newcastle Upon Tyne, UK, pp. 345-350. https://doi.org/10.1109/ICSAE.2016.7810215
[14] Osama, M., Shyaa, A.K. (2025). Passive cooling with combined windcatcher-solar chimney systems: A review paper. International Communications in Heat and Mass Transfer, 169: 109510. https://doi.org/10.1016/j.icheatmasstransfer.2025.109510
[15] Sirror, H. (2024). Innovative approaches to Windcatcher design: A review on balancing tradition sustainability and modern technologies for enhanced performance. Energies, 17(22): 5770. https://doi.org/10.3390/en17225770
[16] Al-Azawiey, S.S., Al-Kayiem, H.H., Hassan, S.B. (2016). Investigation on the influnce of collector height on the performance of solar chimney power plant. ARPN Journal of Engineering and Applied Sciences, 11(20): 12197-12201.
[17] Al-Azawiey, S.S., Hassan, S.B. (2016). Heat absorption properties of ground material for solar chimney power plants. International Journal of Energy Production and Management, 1(4): 403-418. https://doi.org/10.2495/eq-v1-n4-403-418
[18] Pastohr, H., Kornadt, O., Gürlebeck, K. (2004). Numerical and analytical calculations of the temperature and flow field in the upwind power plant. International Journal of Energy Research, 28(6): 495-510. https://doi.org/10.1002/er.978
[19] Sangi, R., Amidpour, M., Hosseinizadeh, B. (2011). Modeling and numerical simulation of solar chimney power plants. Solar Energy, 85(5): 829-838. https://doi.org/10.1016/j.solener.2011.01.011
[20] Abdeen, A., Serageldin, A.A., Ibrahim, M.G., El-Zafarany, A., Ookawara, S., Murata, R. (2019). Solar chimney optimization for enhancing thermal comfort in Egypt: An experimental and numerical study. Solar Energy, 180: 524-536. https://doi.org/10.1016/j.solener.2019.01.063
[21] Fluent, A. (2011). ANSYS Fluent Theory Guide. ANSYS Inc., USA. https://dl.cfdexperts.net/cfd_resources/Ansys_Documentation/Fluent/Ansys_Fluent_Theory_Guide.
[22] Bergman, T.L. (2011). Fundamentals of Heat and Mass Transfer. John Wiley & Sons.
[23] Jamil, I.E.A., Al-Kayiem, H.H., Al-Azawiey, S.S., Shyaa, A.K. (2024). Critical interpretation and analysis to correlate the canopy height to collector diameter ratio for optimized design of solar chimney power plants. International Journal of Renewable Energy Development, 13(1): 99-109. https://doi.org/10.14710/ijred.2024.57689
[24] Duffie, J.A., Beckman, W.A. (1980). Solar Engineering of Thermal Processes. New York: Wiley.
[25] Menni, Y., Azzi, A., Chamkha, A.J. (2018). A review of solar energy collectors: Models and applications. Journal of Applied and Computational Mechanics, 4(4): 375-401. https://doi.org/10.22055/jacm.2018.25686.1286
[26] Shyaa, A.K., Sadiq, G.A. (2026). Numerical and experimental investigation of fin angle influences compact heat exchanger efficiency. Heat Transfer, 55(1): 101-119. https://doi.org/10.1002/htj.70061

NOMENCLATURE

Abbreviations

HT	Heat Transfer
HTP	Heat Transfer Performance
SC	Solar Chimney
CHT	Convection Heat Transfer
AP	Absorber Plate
SCPP	Solar Chimney Power Plant
HF	Heat Flux
SR	Solar Radiation
SE	Solar Energy
TES	Thermal Energy Storage
PCM	Phase Change Material
CFD	Computational Fluid Dynamics
FEA	Finite Element Analysis
NC	Natural Convection
HLC	Heat Loss Coefficient
HTC	Heat Transfer Coefficient
PI	Performance Indicator
SI	Solar Intensity

Nomenclature

AC	Solar Collector Area (m^2)
Ach	Cross-Sectional Area of Solar Chimney (m^2)
CP	Specific Heat of Air (J/Kg.K)
Dh	Hydraulic Diameter (m)
h	Heat Transfer Convection Coefficient (W/m^2. K)
hw	The Wind Heat Transfer Coefficient (W/m^2. K)
IT	Total Solar Radiation on the Surface (W/m^2)
K	Thermal Conductivity (W/m.K)
M*	Mass Flow Rate (Kg/sec)
N	Number of Glasses Covers
Nu	Nusselt Number
qu	Useful Heat Gain of Air in the Collector (W/m^2)
Re	Reynolds Number
S	Absorbed Solar Radiation (W/m^2)
Ta	Ambient Air Temperature (K)
Tc	Cover Temperature (K)
Tf	Air Inside Collector Temperature (K)
Tp	Absorber Plate Temperature (K)
T0	Air Temperature at Collector Outlet (K)
V	Air Velocity in the Collector (m/sec)
Vch	Air Velocity at the Chimney Inlet (m/sec)

Greek symbols

Ηc	Collector Efficiency
α	Absorber Plate Absorptivity
ε	Emissivity of the Cover Glass
ε	Emissivity of the Absorber Plate
ρ	Air Density (Kg/m^3)
μ	Air Dynamic Viscosity ($N \cdot sec/m^2$)
σ	Stefan–Boltzmann Constant (5.67×10^{-8} $W/m^2. K4$)
τ	Glass Transmittance